Quasi-3-D Simulation of High-Brightness Tapered Lasers

Luis Borruel, Slawomir Sujecki, Pablo Moreno, James Wykes, Michel Krakowski, Bernd Sumpf, Phillip Sewell, Sophie-Charlotte Auzanneau, Hans Wenzel, Daniel Rodríguez, Trevor M. Benson, Eric C. Larkins, *Member, IEEE*, and Ignacio Esquivias, *Member, IEEE*

***Abstract*—We present a simulation tool useful to optimize the design of semiconductor tapered lasers and to study the physical processes inside of them. This is achieved by using a state-of-the-art quasi-three-dimensional (quasi-3-D) electrical and thermal model, coupled to a two-dimensional (2-D) wide-angle beam propagation method optical model. A calibration procedure of model parameters is proposed to contribute to the development of reliable simulation tools. Different laser diodes with a tapered gain section, emitting at 735 and 975 nm, are used to validate the model through the extensive comparison of experimental and simulated results. The suitability of 2-D and 3-D electrical, thermal, and optical models is discussed in terms accuracy and computational effort.**

***Index Terms*—Beam quality, filamentation, high-brightness lasers, laser modeling, tapered lasers.**

I. Introduction

HIGH-BRIGHTNESS semiconductor laser sources are one of the most promising devices for current and future applications in the optoelectronics industry. Like other semiconductor lasers, they have incomparable features like small size, high conversion efficiency and low cost. In addition, the superior beam quality of these devices improves their performance for some applications, such as coupling high power into an optical fiber. Broad-area (BA) lasers have demonstrated the highest output power, but the beam quality provided at high power is poor. Tapered lasers, also called flared unstable cavity lasers, are one of the many different designs proposed to achieve a high power-high brightness semiconductor source (see [1]–[3] and references herein). Tapered lasers are currently the most straightforward devices for achieving high brightness at moderate cost, due to the technological simplicity of their fabrication. In fact, the number of research groups reporting tapered lasers with high output powers and improved beam quality at different wavelengths is continuously expanding [4]–[12].

Manuscript received November 18, 2003; revised January 23, 2004. This work was supported by the European Commission through the IST Project 1999-10356, ULTRABRIGHT and Spanish CICYT through Project TIC1999-0645 and Project TIC2000-2030-CE.

L. Borruel, P. Moreno, D. Rodríguez, and I. Esquivias are with the Departamento de Tecnología Fotónica, Universidad Politécnica de Madrid, Madrid 28040, Spain (e-mail: luis@tfo.upm.es).

S. Sujecki, J. Wykes, P. Sewell, T. M. Benson, and E. C. Larkins are with the School of Electrical and Electronic Engineering, University of Nottingham, Nottingham NG7 2RD, U.K.

M. Krakowski and S.-C. Auzanneau are with Thales Research and Technology France, Domain de Corbeville 91404 Orsay, France.

B. Sumpf and H. Wenzel are with the Ferdinand-Braun-Institut für Höchstfrequenztechnik, D-12489 Berlin, Germany.

Digital Object Identifier 10.1109/JQE.2004.826424

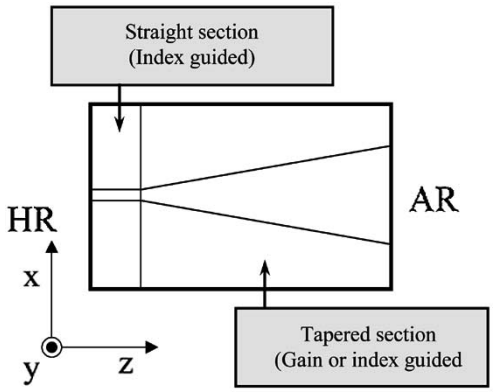

Fig. 1. Schematic view of a tapered laser.

Tapered lasers consist of a ridge waveguide (RW) section and a tapered section (see Fig. 1). The role of the straight section is twofold: it provides a single spatial mode, which is launched into the tapered section, and it filters out the radiation coming from the backward traveling reflected field. The single-mode pattern diffracts during the propagation along the tapered section, lowering the optical density while maintaining the beam quality. The comparatively low optical density reduces the impact of nonlinear phenomena related to the spatial hole burning (SHB) effect, and also reduces catastrophic optical damage (COD) at the laser facet.

Two clearly different types of tapered sections have been reported to date: large gain-guided tapers with a taper angle close to the free diffraction angle [1], [2], [4]–[12], and narrow index-guided tapers with small angle $(<1^\circ)$ [3], [9]. In both cases, beam deterioration due to nonlinear effects, such as self-focusing and filamentation, is the practical limiting factor at high power (i.e., they are not limited by COD). Proper design of both the epitaxial structure and the geometry (relative section lengths and aperture angle) is essential to delay the onset of filamentation in a tapered laser. However, although the basic ideas behind tapered laser design are simple, the complete underlying physics is complex. Accurate simulation models are desirable not only to understand the strong nonlinear phenomena involved, but to demonstrate reliable predictive capabilities and help device manufacturers to improve designs. To achieve this goal in a practical way, it is not sufficient to develop an accurate simulation model. Rather, it is also necessary for the simulation procedure to rely upon a limited number of calibration parameters.

Several groups have previously published simulation models solving the optical, electrical, and thermal equations for

tapered amplifiers [13], [14] and tapered lasers [3], [7], [8], [11], [15]–[18], with different types of approximations. Up to now, the publications describing models for this type of lasers have provided only limited comparisons with experimental results, making difficult a clear verification of their validity for design applications. We have developed a quasi-three-dimensional (quasi–3-D) model solving the bipolar electrical and thermal steady-state equations, coupled to a two-dimensional (2-D) wide-angle finite-difference beam propagation method (WA-FDBPM) model to accurately solve for the optical field distribution. Some of the features of this CW model have been partially described in previous contributions [19]–[21], and the key nonlinear phenomena were identified in [19]. Here we describe with more detail the terms included in the model, the numerical implementation details, and the parameter calibration procedure and validate the model by comparing with experiments in three different types of devices. The simplifications of the model rely on a single-frequency steady-state approach. However, the good results obtained over a wide range of conditions confirm its validity until the beam instabilities appear.

This paper is organized as follows. In Section II, we describe in detail the model and the numerical approaches. In Section III, we describe the experimental devices and the parameter calibration procedure, and we compare simulations with experimental results. In Section IV, we discuss the suitability of 3-D versus 2-D models and we apply the modeling results to analyze the beam properties of the devices under study. Finally, the main conclusions are summarized in Section V.

II. Modeling

A. Model Overview

The numerical solution of the complete semiconductor equations, the vectorial wave equation and the heat flow equation for a tapered laser, is currently a problem needing extremely high computer resources. For this reason, a number of assumptions are necessary to produce a practical simulation model, but without missing the main physical mechanisms governing the device.

The model solves self-consistently the complete steady-state electrical, thermal, and optical equations for the unstable resonator. In order to reduce the complexity of the problem, we solve the 2-D electrical and thermal equations for the vertical-lateral plane (YX plane, see Fig. 1) at different positions along the longitudinal axis (Z axis). The model can include the interaction between YX slices (longitudinal carrier and heat flow), but we have verified that the longitudinal flow of carriers can be neglected in these devices, whereas the longitudinal heat flow has a certain impact on the overall heating (see Section IV), but does not significantly affect the lateral temperature profile. A 2-D wide-angle finite-difference beam propagation method (WA-FDBPM) algorithm, making use of the effective index approximation, is used to propagate the optical field in the XZ plane. This approach has already been proven to be valid in comparison with a complete 3-D BPM model for the structures reported here [21]. A detailed description of the original approach used to couple the electrothermal and optical equations is given in Section II-E.

Two different approaches have been implemented regarding the lateral direction: 1) a full-space model and 2) a half-space model assuming lateral symmetry. The first option makes it possible to simulate beam asymmetries at the expense of a higher computational effort. The choice depends on the structure and the operating conditions of the device under study. The results obtained in the structures presented here are coincident.

The bias voltage is the input parameter defining the injection conditions. Our quasi-3-D model is assisted by a one-dimensional (1-D) simulator that provides, for each bias, initialization data and the emission wavelength, which is kept constant.

B. Electrical Model

The electrical model is based on the self-consistent solution of the Poisson and continuity equations for electrons and holes within different XY planes as follows:

$$\nabla(\varepsilon_d \nabla\phi) + q(p - n + N_D - N_A) = 0 \tag{1}$$

$$\nabla \mathbf{j_n} - q\left(R_{\rm nr} + R_{\rm sp} + F_n^{\rm qw}\right) = 0 \tag{2}$$

$$\nabla \mathbf{j_p} + q\left(R_{\rm nr} + R_{\rm sp} + F_p^{\rm qw}\right) = 0. \tag{3}$$

Two additional continuity equations are formulated for each quantum well (QW) to account for the interactions between the confined and unconfined carrier populations as follows:

$$\int_{\rm qw} F_n^{\rm qw} dv - \left(R_{\rm nr}^{\rm qw} + R_{\rm sp}^{\rm qw} + R_{\rm st}\right) = 0 \tag{4}$$

$$\int_{\rm qw} F_p^{\rm qw} dv - \left(R_{\rm nr}^{\rm qw} + R_{\rm sp}^{\rm qw} + R_{\rm st}\right) = 0 \tag{5}$$

where the terms $F_n^{\rm qw}$ and $F_p^{\rm qw}$ are the net capture/escape rates according to the model described in [22]. Nonradiative recombination $(\mathrm{R_{nr}})$—including Shockley–Read–Hall (SRH) and Auger—and spontaneous recombination $(\mathrm{R_{sp}})$ terms are included along the complete device, in addition to the stimulated recombination in the active region $(\mathrm{R_{st}})$. The model also includes free carrier absorption and bandgap renormalization with standard dependencies and parameters extracted from the literature. A more complete description of the terms included in the equations, as well as the numerical procedures, can be found elsewhere [19], [20], [23], [24].

The material gain and spontaneous recombination rate in the QWs are calculated assuming parabolic bands and Lorentzian broadening. In Section III-B, we describe our approach to take into account band-mixing effects within a parabolic band model. The local material gain (or absorption) is calculated at the lasing wavelength for each point of the mesh, taking into account the local temperature and quasi-Fermi levels.

The electrical equations are solved in the volume defined by the total thickness of the epitaxial layers, cavity length, and chip width. Voltage-controlled ohmic contacts are assumed for the boundary conditions [24] at the epilayer–metal and epilayer–substrate interfaces, and zero normal current at the chip edges. The input data for the equations are taken from material databases according to the epilayer structure. Etched and implanted regions are simulated by assuming negligible carrier mobility.

The equations are discretized using a finite difference approach and separate, nonuniform, meshes for the Y and X axes. The denser regions in the Y and X axes correspond to the QW and to the border of the implanted/etched areas, respectively. The X mesh depends on the longitudinal position, with typically around 50 mesh points. We chose 100 μm for the XY slice separation, having checked that the results in our structures were similar for smaller separations. The numerical procedure used to solve the system of equations can be found elsewhere [20], [25]. When convergence is reached, complete 3-D maps are produced of the electrical variables (electrostatic potential and quasi-Fermi energies for electrons and holes), consistent with the photon and temperature distributions. Carrier and current densities are easily derived using standard expressions. We should stress that this approach properly considers the current spreading and the nonuniformity of the injected current density; two features that are needed to accurately model the SHB effect.

C. Thermal Model

The 2-D heat-flow equation is solved at each XY slice

$$\nabla(\kappa\nabla T) + w(x,y) = 0 \tag{6}$$

where the term for the local heat sources, $w(x,y)$, takes into account: 1) Joule heating; 2) nonradiative (SRH and Auger) recombination; 3) photon absorption by free carriers; and 4) a heat-source, arising from the so-called excess power, needed to fulfill the energy conservation. The excess power mainly accounts for the spontaneous and the scattered laser emission that is absorbed inside the cavity. To validate this approach, we have quantitatively checked that the obtained excess power is in good agreement with the integrated spontaneous and the laser scattered emission power. This heat source is spatially distributed according to the transparency properties of the substrate. More details can be found in [20] and [23].

In addition to the epilayer, the substrate, the metal layers, and the heat sink are also considered in the thermal solution. The boundary conditions used with the heat flow equations in the case of a p-down-mounted laser are: negligible heat flow at the n-metal and lateral chip external interfaces, and uniform room temperature at the bottom of the heat sink. The local heat flow toward the heat sink is controlled by the thickness of the copper heat sink, which is used as a fitting parameter to reproduce the measured average heating of the active layer. In this way, we do not need to consider the heat spreading in a real heat sink, which is larger than the semiconductor chip, thereby reducing the size of the computational window. Etched regions are thermally simulated by introducing the thermal conductivity of the planarization isolator.

The heat flow equation is discretized with a finite difference method, and the system of equations is solved by using a stabilized biconjugate gradient method. When the longitudinal flow is taken into account in (6), an iteration loop sweeping the longitudinal direction is implemented, until a stable solution for the temperature is produced.

D. Optical Model

The optical model is based upon the finite-difference beam propagation method, using wide-angle formulations based upon successive Padé approximations. The effective index method is used to approximate the original 3-D taper structure by a 2-D structure in the XZ plane. At the edge of the analysis window, the perfectly matched layer (PML) boundary condition has been implemented. The phase component of the optical field is conserved at each complete roundtrip. The propagation step for the WA-FDBPM is typically set to 1/50 of the electrical slice separation. The beam spoilers have been represented by setting the field to zero at the beam spoiler location, similar to the procedure used in [15]. More details on the optical model can be found in [19].

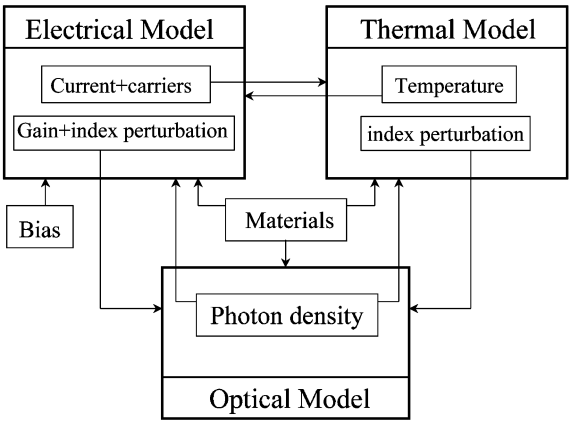

Fig. 2. Input/output interface of the electrical, thermal, and optical models.

E. Coupling Between Models

The coupling of the electrical, thermal, and optical equations is critical for obtaining a stable solution in unstable cavity resonators. Our model has been implemented using a modular structure in which an input/output interface is defined for each module, making it easy to implement different coupling schemes. The interfacing between the different modules is illustrated in Fig. 2. The execution flow, denominated coupled solution method [26], consists of the following module interaction.

1) The electrical model solves a given XY plane located at a longitudinal position $z = j$ and corresponding to the k-th propagation trip. It makes use of the photon density distribution provided by the optical model and of the calculated temperature distribution from the $k-1$ propagation trip. In the case of $z = k = 1$, the initial guess of the optical field is based on the profile of the fundamental mode of the waveguide. In addition, the electrical model assumes an isothermal temperature distribution for $k = 1$.
2) The heat sources are calculated and the heat flow equation is solved using the electrical solution as input, yielding the XY temperature distribution at $z = j$. This distribution is not used to recalculate 1) according to an electrothermal loop. Instead, the distribution is used the next time the electrical module solves this slice (i.e., $k = k + 1$).
3) The real and imaginary parts of the dielectric constant perturbation are calculated using the results from 1) and 2), according to the formulation detailed at the end of this section.

4) The optical field is propagated from $z = j$ to $z = j+1$ or $j-1$ (depending on whether k is a forward or backward propagating trip) with the data provided by 3). When the propagation process reaches one of the mirror facets, a reflection coefficient is applied and a new propagating trip starts. The loop is closed when the resulting optical field is delivered to 1).

After several roundtrips along the cavity (typically five to ten), a stable self-consistent solution for the optical field, carrier, and temperature distributions along the complete cavity is found. The convergence criterion is based on the stability of the optical field at the back facet, both in shape and power, after two consecutive round trips. It is mathematically expressed by the parameter ε as follows:

$$\varepsilon = \frac{\langle |f_n - f_{n-1}|, |f_n - f_{n-1}| \rangle}{\langle |f_n + f_{n-1}|, |f_n + f_{n-1}| \rangle} \tag{7}$$

where f_n is the optical field at the rear facet after n round trips, and $\langle , \rangle$ denotes scalar product. The iterative process ends when ε is lower than a user-specified threshold value.

Once we have obtained a stable solution, a complete set of output results is generated: 1) output power by integrating the optical field at the output facet; 2) input current by integrating the current density at the p- or n-metal surfaces; and 3) a collection of figures of merit (far-field (FF) divergence, M^2 parameter, astigmatism, and virtual source width), calculated after postprocessing of the final optical field distribution.

However, the convergence criterion may not be fulfilled for all bias conditions. The laser designs studied up to date yield a stable solution up to a certain value of the injection current (bias voltage). Any further increase in current makes the convergence process slower, due to the onset of filamentation, and at even higher currents fails to convergence altogether. This lack of convergence is associated either with a wandering shape of the field or to a gradual power reduction. The convergence properties are quite dependent on the details of the device structure. The absence of convergence appears to be related to the observation of beam filamentation and power saturation at high injection levels.

To ensure a good reproduction of the physical processes leading to filamentation, it is important to properly define the local perturbation of the dielectric function caused by carriers and temperature. Unlike most previous models, we characterize independently the variations of the refractive index and of the material gain, instead of using a single value for the linewidth enhancement factor. The gain provided to the optical model is calculated taking into account the local material gain, the vertically integrated free-carrier absorption losses, and the scattering losses. The perturbation of the effective refractive index $\delta n_{\text{eff}}(x,z)$ takes into account carrier– and temperature-induced changes as follows:

$$\delta n_{\text{eff}}(x,z) = \delta n_T[T(x,z)] + \delta n_N[N(x,z)] \tag{8}$$

where $T(x,z)$ is the active layer temperature. We calculate the temperature-induced change $\delta n_T[T(x,z)]$ with a linear dependence

$$\delta n_T[T(x,z)] = \frac{\partial n}{\partial T} \times (T(x,z) - T_{\text{RT}}) \tag{9}$$

TABLE I
GEOMETRICAL PARAMETERS OF THE DEVICES UNDER STUDY

Device	A	B	C
Wavelength (nm)	975	975	735
Guiding (tapered section)	Index	Gain	Gain
Taper full angle (°)	< 1	4	4
Ridge waveguide length (μm)	200	500	750
Beam spoilers	No	Yes	No

where T_{RT} is the room temperature. The carrier-induced refractive index perturbation $\delta n_N[N(x,z)]$ considers the contribution of QW carriers and a nonlinear dependence as follows:

$$\delta n_N[N(x,z)] = n_1 \sum_i \sqrt{N^i(x,z)}\Gamma_V^i \tag{10}$$

where N_i and Γ_V^i are the carrier concentration and vertical confinement factor, respectively, at the ith QW and n_1 is a negative coefficient determining the index variation. The square root function in (10) has been chosen after analyzing our own measurements [27], other published experimental results [28], and theoretical calculations [29]. The coefficient n_1 has been used as a fitting parameter, which is kept constant for a particular epitaxial device structure. The wavelength and temperature dependencies of the carrier induced index variations have not been considered.

III. MODEL VALIDATION

A. Experimental Devices

Three different device geometries, at two different wavelengths, with a common cavity length of 2 mm are used in this work: A) 975 nm laser with a small-angle index-guided tapered section; B) 975 nm laser with a large-angle gain-guided tapered section; and C) 735 nm laser with a large-angle gain-guided tapered section. The most important geometrical parameters of these devices are summarized in Table I.

Devices A and B were fabricated with identical epitaxial structures, which are described in more detail in [9]. In brief, the laser structure consists of a strained InGaAs QW embedded in InGaAsP confinement layers and InGaP cladding layers. The 735-nm laser structure consists of a tensile strained GaAsP QW with AlGaAs confinement and cladding regions [10], [30]. Both designs employ a large optical cavity to reduce the fast axis divergence and to decrease the tendency to filamentation, with similar values for the vertical confinement factor. The technological details related to the device fabrication were slightly different for the two material systems, including in both cases etching to define the index guided sections, and ion-implantation to define the injection area. Antireflection (∼5%) and high reflection (∼90%) coatings were applied to the front and back facets, respectively. The devices were mounted p-side down on passive heat sinks. BA lasers with contact widths of 100 μm and different cavity lengths were also fabricated to assess the material quality and for the determination of simulation parameters, as will be described later.

The main design difference between the two devices with a large gain-guided tapered section and different emission wavelengths (devices B and C) was the presence of beam spoilers in the case of the 975-nm laser (device B). The beam spoilers were fabricated by etching grooves adjacent to the RW structure, down through the active region and angled to deflect unwanted radiation. The grooves were placed at the end of the RW section adjoining the tapered section and acts as a spatial filter.

A complete characterization procedure was applied to the fabricated laser devices at room temperature and under CW conditions. It included the measurement of power–voltage–current characteristics, FF patterns for the fast and slow axes, near-field (NF) patterns at the output facet and at the beam waist, beam astigmatism, and beam quality parameter M^2 ($1/e^2$ definition).

B. Simulation Parameters and Fitting Procedure

Most of the simulation parameters employed in the simulations for AlGaAs and InGaAs (bandgap, mobilities, refractive indexes...) were taken from standard references [31], [32] when properly known. The InGaAsP bandgap energy was estimated from photoluminescence measurements, and a value of 0.65 was assumed for the conduction band offset in the InGaAs–InGaAsP heterojunction of 975-nm devices. The band alignment presented in [30] was employed for the GaAsP–AlGaAs QWs. A value of 2×10^{-30} cm$^6\cdot$ s^{-1} was used for the electron and hole Auger coefficients, based on GaAs values [31]. The electron and hole free carrier absorption coefficients were 3×10^{-18} cm^2 and 7×10^{-18} cm^2, respectively, also based on GaAs values [33].

The first stage of the calibration procedure involves the correction of the parameters used in the parabolic band model, to take into account band-mixing effects with low computational effort. We fitted the maximum material gain and spontaneous recombination current versus carrier density relationships calculated using parabolic bands to numerical results obtained from an eight-band $\boldsymbol{k\cdot p}$ theory [31]. The input parameters were the QW energy levels and effective masses, together with two scaling parameters for the $g_{\rm mat}(n)$ and $R_{\rm sp}(n)$. Very good agreement was achieved for a wide range of carrier densities.

The next step in the calibration procedure was to determine those parameters related to the material quality (internal losses and SRH recombination parameters) by means of BA laser measurements. We compared 1-D simulations with experimental results in terms of threshold current density $J_{\rm th}$ dependence on the cavity length L, internal quantum efficiency $\eta_{\rm in}$, internal losses $\alpha_{\rm in}$, and characteristic temperature T_0.

The value of $\eta_{\rm in}, \alpha_{\rm in}$, and characteristic temperature T_0 was extracted from the experimental data using standard procedures [31], and the same treatment was applied to the simulated results.

In the case of 975-nm devices, the best agreement was achieved by including SRH recombination in the QW region and 0.3 cm^{-1} for the scattering losses, yielding 1.4 cm^{-1} for the total internal losses. In the case of 735-nm lasers, SRH recombination was included in the graded index heterostructure (GRIN) region, instead of the QW, and no scattering losses were considered (the calculated free carrier absorption losses accounted for the measured internal losses). Table II compares the results of 1-D simulations and experimental results for BA lasers fabricated in both material systems. Good general agreement was found for the optoelectronic properties, as well as for the voltage–current characteristics.

TABLE II
COMPARISON OF EXPERIMENTS AND SIMULATIONS FOR BA LASER PARAMETERS

	Exp. (975 nm)	Model (975 nm)	Exp. (735 nm)	Model (735 nm)
Jo (A/cm²)	64	71.1	170	176
Γ *Go (cm⁻¹)*	14.5	13.5	24.6	26.4
To (°K)	127	122.6	66	66
η_{in} *(%)*	94	92	83	84
α_{in} *(cm−1)*	1.5	1.4	0.6	0.8

The final stage of the calibration procedure has two parameters: one to account for the carrier-induced refractive index change and the other one to account for the heat transfer efficiency. For the first one, we focused on the main effect of the carrier lensing, trying to achieve a good agreement between simulations and experiments in terms of the beam divergence at a fixed output power. This was achieved by using the coefficient n_1 as fitting parameter, relating the index change and carrier density in expression (10). Values of -4.1×10^{-11} cm$^{3/2}$ and -2.7×10^{-11} cm$^{3/2}$ for n_1 provided simulated FF patterns similar to those measured at high power for devices A and C, respectively. These values were used for the simulation of all devices with the corresponding epitaxial structures. The fitted value of n_1 for the 975-nm devices was similar to the value we measured in BA lasers [27] $-4.7\ 10^{-11}$ cm$^{3/2}$.

We found that the thickness of the copper heat sink was the best fitting parameter to reproduce the measured values of the active region temperature; in this way, we defined the total value of the device thermal resistance. However, we could not measure the spatial temperature distribution, but only to estimate the average temperature increase from the shift of the lasing wavelength (assuming a standard dependence). In consequence, we simply modified the fitting parameter to achieve a temperature increase (on average) roughly similar to the experimental value. It was observed that, by changing the heat sink thickness, we shifted the absolute value of the temperature without important modifications to the shape of the lateral and longitudinal temperature profiles.

C. Model Validation: Simulations Versus Experiments

Fig. 3 shows the experimental and simulated optical power–current (*P–I*) characteristics of the three laser structures. The agreement between experiments and simulations in terms of threshold current and slope efficiency was fairly good, particularly taking into account that our fitting procedure was only related to the properties of BA lasers and to the FF patterns at a single power, and that constant values for these parameters were used for each material system. The maximum powers for the experimental *P–I* curves in Fig. 3 were not limited by the setup or by COD, but they correspond to a saturation value, indicating a physical limit. In the case of the simulations, the maximum power shown in Fig. 3 corresponds to the maximum bias current yielding a stable solution: at higher bias currents, we did not

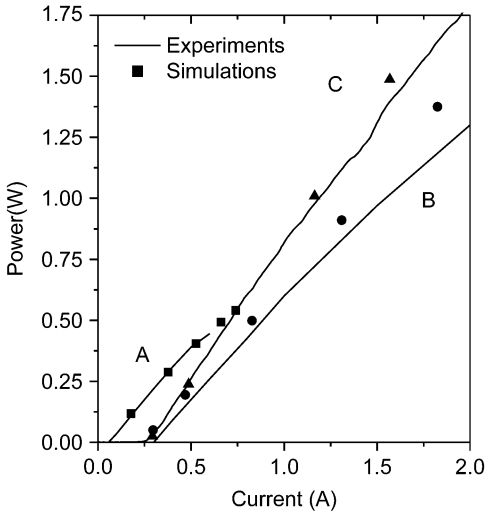

Fig. 3. Simulated and experimental power–current response for devices A, B, and C.

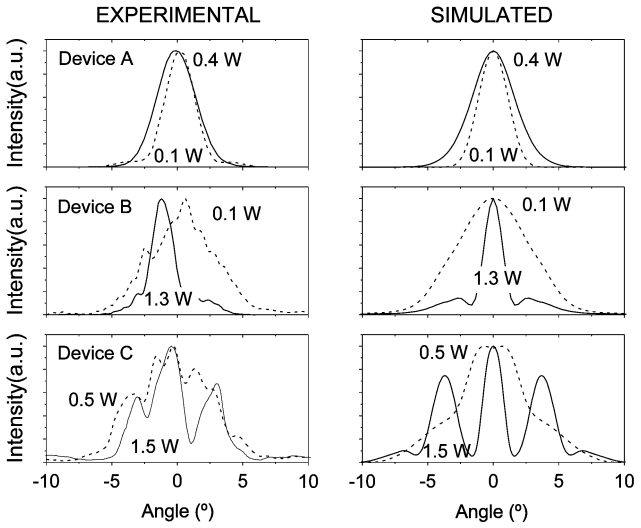

Fig. 4. Comparison of the experimental and simulated FF patterns at low and high output power for devices A, B, and C.

achieve convergence, but a reduced output power and narrower beam profile at each iteration step. The values for the maximum power in simulations agreed fairly well with the measured values. We conclude that the main physical mechanism limiting the maximum power is properly reproduced in the simulations. Similar experimental behavior was reported by Donnelly *et al.* [34] in 1.5-μm lasers with a tapered gain-guided region.

Some examples of measured and simulated FF patterns (without the corrections for the quadratic phase curvature usually made in the literature) are shown in Fig. 4 for the three devices under study at two different power levels. It can be observed that the shape and evolution with output power of the FF patterns are completely different for the three devices under study, as discussed later in Section IV-B. In spite of this, the global agreement between simulations and experiments is very good, especially taking into account that the exact pattern for device C is device-dependent, which makes the comparison more difficult. The measured and simulated evolution of the FF divergence of devices A and B, and the evolution of the

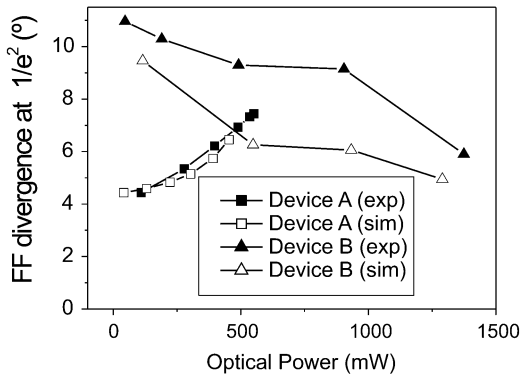

Fig. 5. Comparison of the experimental and simulated FF divergence (at $1/2$) versus output power for devices A and B.

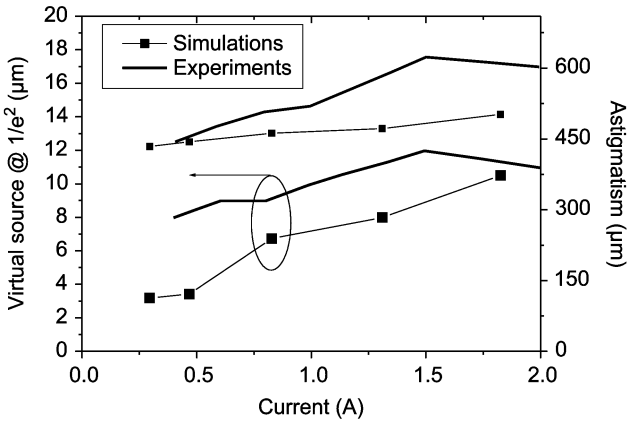

Fig. 6. Comparison of the experimental and simulated virtual source width at $1/e2$ and astigmatism as a function of the injection current for device B.

beam waist, and the astigmatism for device B are compared in Figs. 5 and 6 as the output power is increased. A detailed comparison between simulations and experiments for device C has been previously reported in [19]. In all cases, the simulations follow same trends than the experiments, with good qualitative agreement and some differences in quantitative parameters in device B (see Figs. 5 and 6). We conclude that the numerical model and calibration procedure correctly account for the main physical effects determining the beam properties.

IV. Discussion

A. Need and Limits of a Quasi-3-D Model

Any numerical model of a semiconductor device must consider the balance between how completely it describes physical processes and its applicability due to limited computer resources and complexity of input parameters. In this section, we analyze this balance in the model previously described with the aim of justifying the need for a quasi-3-D model for the simulation of tapered lasers, but being aware of the limitations of the steady state and single wavelength assumptions.

Previous publications reporting dynamical models [16], [18] have pointed out the nonlinear dynamic interaction between the gain medium and the optical field and its role in filamentation phenomena and spectral characteristics in semiconductor lasers. However, a complete quasi-3-D time-dependent and spectrally

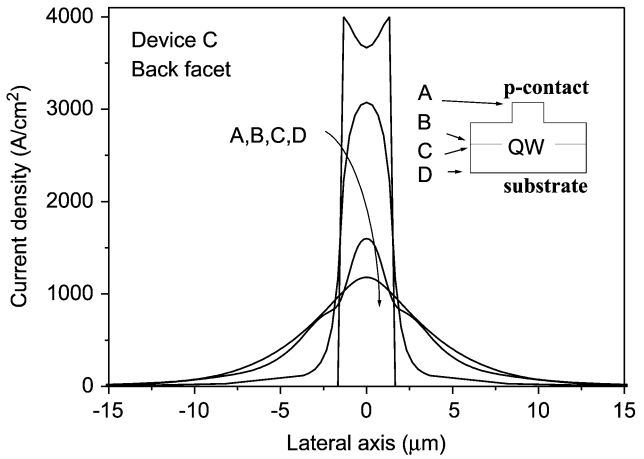

Fig. 7. Lateral pattern of the electrons and holes current density $\mathbf{J_y}$ at four different positions in the epitaxial structure.

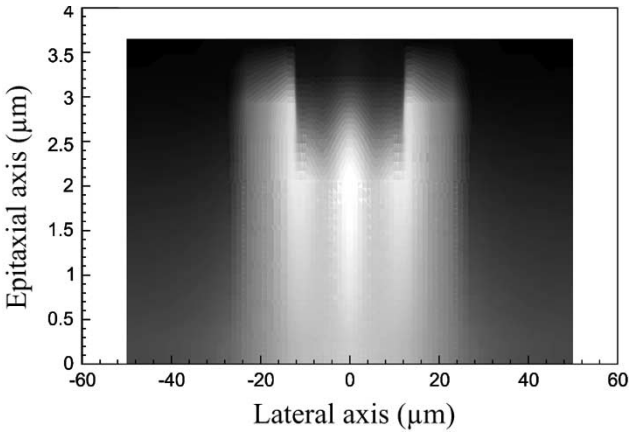

Fig. 8. Temperature map of device A at the RW section. The range shown goes from $T \sim 36°$C (black) to $T \sim 39\,°$C (white).

resolved model would need extremely high computer resources. The goal of our model is to analyze the CW beam properties at high power levels, and to contribute to improve the geometrical designs; in consequence, our steady-state single-frequency approach is an adequate compromise between applicability and complexity, as demonstrated by the good agreement between experiments and simulations shown in previous section.

The group of Lang *et al.* [13] presented the first numerical model of a flared semiconductor amplifier, which included a simplified gain model together with a BPM for the optical field, and a thermal model. Their model predicted the enhanced performance of flared devices, which was later experimentally demonstrated [5]. Subsequent models by different groups [3], [7], [8], [11], [15]–[18] expanded Lang's work improving the electrical equations, considering in some cases dynamical effects, and including tapered lasers. The main difference between this work and previously published models for tapered lasers (steady state or dynamical), is the inclusion, for the first time, of the vertical direction in the thermal and electrical solutions. In the following paragraphs, we justify the importance of a complete solution of the laser cross section, especially in the simulation of the RW section. Previous 2-D models for RW lasers [35] have already pointed out the need to consider 2-D current flow.

The use of a 1-D standard unipolar diffusion equation for the lateral direction in the QW plane implies a flat or assumed current injection profile, clearly limiting the precision to reproduce current spreading and SHB, which are key phenomena in tapered lasers. In order to stress the need to accurately simulate this dimension, we have plotted in Fig. 7 the lateral distribution of the vertical current density ($\mathbf{J}_y$) for the RW section of device C at four different positions along the epitaxial structure. In the graph, we can see that the width of the injected region is determined by current spreading along the RW section, and by the carrier diffusion in the QW, with noticeable differences between the electron and hole injection profiles (not shown). After a high number of tapered laser simulations, we have verified that the resulting current distribution (and, in consequence, the gain and index profiles) depends strongly upon the epitaxial structure, the etch depth, and the recombination processes in the QW. Furthermore, the resulting injection profile depends on the bias level, making it very difficult to account for all these mechanisms with a 1-D model. On the other hand, as we pointed out in Section II-A, the use of a full 3-D electrical model by including the interaction between XY slices does not affect the results. We conclude that our quasi-3-D electrical model (solution of electrically independent device cross sections) is the best compromise between accuracy and computational efficiency.

The lack of a complete 3-D map of the electrical variables implies a limited calculation of the local heat sources. As a consequence, most of previous models for tapered lasers only attempt to solve for the lateral temperature distribution using Lang's model [13]. The model reported in [15] includes the complete 3-D thermal solution, but the heat sources are calculated from a 1D electrical model. A fully 3-D thermal model has two main advantages: to account for the longitudinal flow of heat and to properly simulate nonuniformities in the vertical direction, e.g., the isolators introduced in the etched regions.

The complete solution of the thermal problem is of critical importance for the index guided sections. For instance, in devices A and B a polymer with low thermal conductivity was used as the planarization isolator in the etched regions. Although these regions are only several micrometers wide, the heat flow toward the heat sink is modified and the resulting temperature profile is clearly 2-D. This effect is illustrated in Fig. 8, where we have plotted the temperature distribution at the output facet of device A for an output power of 0.4 W.

The influence of including the longitudinal heat flow in the solution can be appreciated in Fig. 9. In the upper part we show the QW temperature distribution without longitudinal heat flow (quasi-3-D), while in the lower part this term was considered in the equations (full 3-D). The lateral temperature gradient, which is the most important thermal parameter affecting the beam properties (due to thermal lensing), is similar in both cases. However, the quasi-3-D solution overestimates the longitudinal temperature gradient (about five degrees for this particular operating condition, $P = 0.4$ W). This difference is not very important in most cases, although it can produce a decrease in the modal gain at high injection conditions, due to the thermal shift of the local gain maximum. We think that a fully 3-D thermal model provides some advantages at a

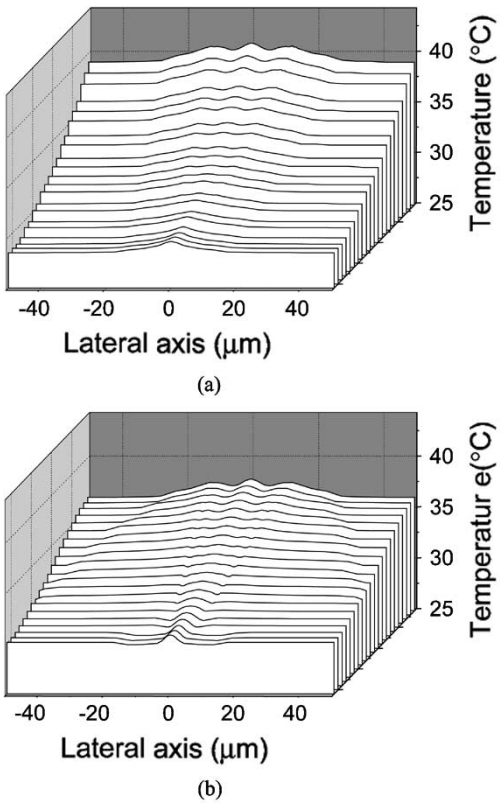

Fig. 9. Temperature map of the QW in device A, neglecting (a) the longitudinal flow and (b) considering it.

reasonable computational cost, but a quasi-3-D thermal model is appropriate for most tapered laser simulations.

In a previous contribution [21], we reported that a 3-D WA-FDBPM optical model shows a little improvement compared to a 2-D WA-FDBPM, whereas the computer resources needed are about one order of magnitude higher.

B. Analysis of the Beam Characteristics

In this section, we discuss the physical insights obtained from the simulation of the three tapered laser structures under study to get a better understanding of their optoelectronic properties. We begin by summarizing the different behaviors observed in the beam properties, both in the experimental and the modeling results.

1) Device A (narrow taper at 975 nm): single-lobed NF and FF patterns with a Gaussian-like shape. The FF divergence increases with increasing power (Fig. 5) and the NF width at the output facet decreases with increasing current.
2) Device B (large taper at 975 nm): astigmatic beam, showing single-lobed FF patterns at low power, with a clear narrowing at the center and small secondary lobes at the highest power (Fig. 4, central row). At 1.3 W output power, 94% of the total power is contained in the central lobe of the beam waist. The width of the virtual source and the astigmatism increase with the output power up to a saturation value, showing an small decrease at the maximum power (Fig. 6). The NF at the output facet narrows with the increasing power (not shown).
3) Device C (large taper at 735 nm): astigmatic beam, with multiple lobes in the uncorrected FF—even at low power (Fig. 4, bottom). Upon increasing the power, a larger number of peaks appear in the uncorrected FF patterns, without any drastic narrowing (see [19] for detailed experimental and simulated results). 75% of the total power is contained in the central lobe of the beam waist even at 1.5 W, and only small secondary lobes are observed. The astigmatism does not increase with the power, and the beam parameter M^2 ($1/e^2$ criterion) increases slowly with the power, with a value of 1.5 at 1.5 W.

Two main topics can be addressed in the comparison of the beam properties: 1) the differences between narrow- and wide-aperture devices with identical epitaxy (A and B) and 2) the differences between devices with similar geometry, but completely different materials (B and C).

1) The simulated QW carrier distribution (not shown) indicates the strong role of SHB at high power in the two 975-nm devices. However, the effect of the carrier-induced parasitic waveguide on the beam divergence is quite different. In the narrow index-guided tapered laser (device A), the beam is diffracting from the approximately 20-μm-wide output aperture, with a very small phase curvature at the facet at low power. By increasing the power, the carrier induced waveguide produces a convergent lens effect during the beam propagation in the tapered region, narrowing the beam at the facet and thus, increasing the diffraction angle. In consequence, the FF divergence increases with power (see Fig. 5). In the case of the large gain guided tapered laser (device B), the beam diffracts at the beginning of the tapered section. It reaches the output aperture with a relatively large phase gradient and at high power, the beam divergence inside the tapered section is counteracted by the parasitic convergent lens effect, in consequence, FF and NF widths are simultaneously reduced.
2) The different beam properties observed between devices B and C are mainly due to: the role of the beam spoilers in the former (improving the RW filtering properties) and the higher inherent tendency to filamentation in the 975-nm material. This is caused by the higher linewidth enhancement factor, arising from a higher differential index and a lower differential gain [36]. A more complete analysis of device C, showing the role of optical pumping and electrical over-pumping effects, can be found in [19].

V. Conclusion

A state-of-the art quasi-3-D optical, thermal, and electronic model has been reported and validated through the simulation of different tapered lasers emitting at 975 and 735 nm. It includes important features, such as electrically solving for the vertical direction and a carrier-dependent dielectric constant. Good qualitative and quantitative agreement between experiment and simulation has validated the modeling approach. The analysis of the device internal variable profiles (carriers, photons, and temperature) yielded by the simulations provided a

good understanding of the beam quality limitations in the different devices.

In order to make the program more usable, a three-step calibration procedure is proposed, which is designed to: 1) balance the limitations of the parabolic band approach; 2) account for the growth quality (which cannot be determined *a priori*); and 3) heating and self-focusing properties of the 3-D device. With this unique procedure, we have achieved good agreement with experiments for different QW materials (975 and 735 nm) over a wide range of emitted powers and guiding conditions. For the first time, the threshold current, external efficiency and FF are successfully reproduced using a single set of calibration parameters obtained by a consistent procedure.

From the comparison of 3-D and 2-D models, we have concluded that quasi-3-D electrical and thermal model, coupled to a 2-D optical model is the best compromise between accuracy and computational efficiency when dealing with CW beam quality. However, the computer resources needed to include beam dynamics and output spectra will be probably affordable in the near future.

REFERENCES

[1] J. N. Walpole, "Semiconductor amplifiers and lasers with tapered gain region," *Opt. Quantum Electron*, vol. 28, pp. 623–645, 1996.

[2] M. Mikulla, "Tapered high-power, high-brightness diode lasers: Design and performance," *High-Power Diode Lasers, Topics Appl. Phys*, vol. 78, pp. 265–288, 2000.

[3] K. A. Williams, R. W. Penty, I. H. White, D. J. Robbins, F. J. Wilson, J. J. Lewandowski, and B. K. Nayar, "Design of high—Brightness tapered laser arrays," *IEEE J. Select. Topics Quantum Electron.*, vol. 5, pp. 822–831, May/June 1999.

[4] E. S. Kintzer, J. N. Walpole, S. R. Chinn, C. A. Wang, and L. J. Missagia, "High-power, strained-layer amplifiers and lasers with tapered gain regions," *IEEE Photon. Technol. Lett.*, vol. 5, pp. 605–607, June 1993.

[5] D. Mehuys, S. O'Brien, R. J. Lang, A. Hardy, and D. F. Welch, "5 W, diffraction-limited, tapered-stripe unstable resonator semiconductor laser," *Electron. Lett.*, vol. 30, pp. 1856–1857, 1994.

[6] S. O'Brien, D. Mehuys, R. J. Lang, and D. F. Welch, "1 W CW single frequency, diffraction-limited unstable resonator semiconductor laser with distributed Bragg reflector mirrors," *Electron. Lett.*, vol. 31, pp. 203–205, 1995.

[7] S. Delépine, F. Gérard, A. Pinquier, T. Fillion, J. Pasquier, D. Locatelli, J. P. Chardon, H. K. Bissessur, N. Bouché, F. R. Boubal, and P. Salet, "How to launch 1 W into single-mode fiber from a single 1.48 μm flared resonator," *IEEE J. Select. Topics Quantum Electron*, vol. 7, pp. 111–123, Mar./Apr. 2001.

[8] S. Kristjansson, N. Eriksson, P. Modh, and A. Larsson, "Grating-based surface-emitting tapered unstable resonator laser simulations and experiments," *IEEE J. Quantum Electron.*, vol. 37, pp. 1441–1448, Nov. 2001.

[9] M. M. Krakowski, S. Auzanneau, M. Calligaro, O. Parillaud, P. Collot, M. Lecomte, B. Boulant, and T. Fillardet, "High power and high brightness laser diode structures at 980 nm using Al-free materials," *Proc. SPIE*, vol. 4651, pp. 80–91, 2002.

[10] B. Sumpf, R. Hülsewede, G. Erbert, C. Dzionk, J. Fricke, A. Knauer, W. Pittroff, P. Ressel, J. Sebastian, H. Wenzel, and G. Tränkle, "High-brightness 735 nm tapered diode lasers," *Electron. Lett.*, vol. 38, pp. 183–184, 2002.

[11] R. Bedford and M. Fallahi, "Semiconductor unstable resonators with laterally finite mirrors," *IEEE J. Quantum Electron.*, vol. 38, pp. 716–723, July 2002.

[12] M. Behringer, M. Philippens, W. Teich, A. Schmitt, J. Heerlein, G. Herrmann, J. Luft, G. Seibold, B. Köhler, T. Brand, and J. Biesenbach, "More brilliance from high power laser diodes," *Proc. SPIE*, vol. 4993, pp. 68–76, 2003.

[13] R. J. Lang, A. Hardy, R. Parke, D. Mehuys, S. O'Brien, J. Major, and D. Welch, "Numerical analysis of flared semiconductor laser amplifiers," *IEEE J. Quantum Electron*, vol. 29, pp. 2044–2051, June 1993.

[14] E. Gehrig and O. Hess, "Spatio-temporal dynamics of light amplification and amplified spontaneous emission in high-power tapered semiconductor laser amplifiers," *IEEE J. Quantum Electron.*, vol. 37, pp. 1345–1355, Oct. 2001.

[15] S. Mariojouls, S. Margott, A. Schmitt, M. Mikulla, J. Braunstein, G. Weimann, F. Lozes, and S. Bonnefont, "Modeling of the performance of high-brightness tapered lasers," *Proc. SPIE*, vol. 3944, pp. 395–406, 2000.

[16] C. Z. Ning, J. V. Moloney, A. Egan, and R. A. Indik, "A first-principles fully space-time resolved model of a semiconductor laser," *Quantum Semiclass. Opt.*, vol. 9, pp. 681–691, 1997.

[17] K. Boucke, J. Rogg, M. Kelemen, R. Poprawe, and G. Weimann, "Numerical simulations of novel high-power, high-brigthness laser diode structures," *Proc. SPIE*, vol. 4646, pp. 586–592, 2002.

[18] A. V. Chelnokov, J.-M. Lourtioz, and P. Gavrilovic, "Numerical modeling of the spatial and spectro-temporal behavior of wide-aperture unstable resonator semiconductor lasers," *IEEE Photon. Technol. Lett.*, vol. 7, pp. 863–865, Aug. 1995.

[19] S. Sujecki, L. Borruel, J. Wykes, P. Moreno, B. Sumpf, P. Sewell, H. Wenzel, T. M. Benson, G. Erbert, I. Esquivias, and E. C. Larkins, "Non-linear properties of tapered laser cavities," *IEEE J. Select. Topics Quantum Electron.*, vol. 9, pp. 823–834, May/June 2003.

[20] L. Borruel, S. Sujecki, I. Esquivias, J. Wykes, P. Sewell, T. M. Benson, E. C. Larkins, J. Arias, and B. Romero, "A selfconsistent electrical, thermal and optical model of high brightness tapered lasers," *Proc. SPIE*, vol. 4646, pp. 355–366, 2002.

[21] J. Wykes, L. Borruel, S. Sujecki, I. Esquivias, P. Sewell, T. M. Benson, E. C. Larkins, P. Moreno, and M. Krakowski, "Hot-cavity modeling of high-power tapered laser diodes using wide-angle 3D-BPM," *Proc. LEOS*, vol. 1, pp. 91–92, 2002.

[22] L. Borruel, J. Arias, B. Romero, and I. Esquivias, "Incorporation of carrier capture and escape processes into a self-consistent cw model for quantum well lasers," *Microelectron. J.*, vol. 34, pp. 675–677, 2003.

[23] J. Arias, L. Borruel, B. Romero, G. Batko, I. Esquivias, R. Gómez Alcalá, J. P. Hirtz, J. Nagle, and P. Collot, "One-dimensional simulation of high power laser diode structures," unpublished.

[24] *Reference Manual, Photon Design*, Harold™, Oxford, U.K..

[25] B. Romero, G. Batko, J. Arias, L. Borruel, I. Esquivias, and R. Gomez-Alcala, "Modeling of facet heating in high power laser diodes," *Proc. SPIE*, vol. 3889, pp. 96–106, 1999.

[26] J. G. Wykes, L. Borruel, S. Sujecki, P. Sewell, T. M. Benson, E. C. Larkins, and I. Esquivias, "Convergence behavior of coupled electromagnetic/electronic high power laser models," in *Proc. IEE CEM*, Bournemouth, U.K., 2002.

[27] D. Rodríguez, L. Borruel, I. Esquivias, M. Krakowski, and P. Collot, "Measurement of gain spectra, refractive index shift and linewidth enhancement factor in Al-free 980 nm lasers with broadened waveguide," *Proc. SPIE*, vol. 4646, pp. 344–354, 2002.

[28] D. J. Bossert and D. Gallant, "Gain, refractive index and a-parameter in InGaAs-GaAs SQW broad-area lasers," *IEEE Photon. Technol. Lett.*, vol. 8, pp. 322–324, Mar. 1996.

[29] H. Wenzel, G. Erbert, and P. M. Enders, "Improved theory of the refractive-index change in quantum-well lasers," *IEEE J. Select. Topics Quantum Electron.*, vol. 5, pp. 637–642, May/June 1999.

[30] G. Erbert, F. Bugge, A. Knauer, J. Sebastian, A. Thies, H. Wenzel, and G. Tränkle, "High-power tensile-strained GaAsP-AlGaAs quantum-well lasers emitting between 715 and 790 nm," *IEEE J. Select. Topics Quantum Electron.*, vol. 5, pp. 780–784, May/June 1999.

[31] L. A. Coldren and S. W. Corzine, *Diode Lasers and Photonic Integrated Circuits*. New York: Wiley, 1995.

[32] S. Adachi, Ed., *Properties of Aluminum Gallium Arsenide*. Stevenage, U.K.: IEE/Inspec, 1993.

[33] H. C. Casey and M. B. Panish, *Heterostructure Lasers*. New York: Academic, 1978.

[34] J. P. Donnelly, J. N. Walpole, S. H. Grove, R. J. Bailey, L. J. Missaggia, A. Napoleone, R. E. Reeder, and C. C. Cook, "High-power 1.5 μm tapered-gain-region lasers," *Proc. SPIE*, vol. 3284, pp. 54–62, 1998.

[35] Z.-M. Li, K. M. Dzurko, A. Delâge, and S. P. McAlister, "A self-consistent two-dimensional model of quantum-well semiconductor laser: Optimization of a GRIN-SCH SQW laser structure," *IEEE J. Quantum Electron.*, vol. 28, pp. 792–803, Apr. 1992.

[36] L. Borruel, S. Sujecki, M. Krakowski, B. Sumpf, P. Moreno, J. Wykes, S. C. Auzanneau, G. Erbert, D. Rodríguez, P. Sewell, M. Calligaro, H. Wenzel, T. M. Benson, E. C. Larkins, and I. Esquivias, "High brightness tapered lasers at 732 nm and 975 nm: Experiments and numerical anal-ysis," in *Proc. IEEE Int. Semiconductor Laser Conf.*, Garmisch, Germany, Sept. 2002, pp. 89–90.

Luis Borruel was born in Madrid, Spain, in 1972. He received the B.Eng. degree in telecommunications from Universidad Politécnica de Madrid, Madrid, Spain, in 1994 and the M.Sc. degree in physics from the Universidad Nacional de Educatión a Distancia (UNED), Spain, in 2000. He is currently working toward the Ph.D. degree at the Universidad Politécnica de Madrid.

In 1998, he joined the Laser Diode group in the Photonics Technology Department, Universidad Politécnica de Madrid. After working on piezoelectric effects in InGaAs quantum-well lasers, his current research interests are in high-brightness laser simulation, optimization, and characterization.

Slawomir Sujecki received the M.Sc. and Ph.D. degrees in electronic engineering from the Warsaw University of Technology, Warsaw, Poland, in 1993 and 1997, respectively.

He spent one academic year (1994–1995) with the Technische Universität Berlin, Berlin, Germany, as a DAAD Fellow and two years (1996–1998) with the University of Nottingham, Nottingham, U.K., as a British Council and then Royal Society/Wolfson Foundation Fellow. In 1998, he was with Kielce University of Technology, Kielce, Poland, and in 1999 he joined the National Institute of Telecommunications, Warsaw, Poland. Since April 200l, he has been with the School of Electrical and Electronic Engineering, University of Nottingham.

Pablo Moreno was born in Spain in 1978. He received the degree in physics from the University Complutense of Madrid, Madrid, Spain, in 2002.

From July 2001 to October 2002, he was a Research Assistant with the Photonics Technology Department, Universidad Politécnica de Madrid. Besides high-power semiconductor lasers, he is presently engaged in research on monolithic mode-locked lasers at high repetition rates.

James Wykes received the M.Eng. degree in electronic engineering (first class honors) from the University of Nottingham, Nottingham, U.K., in 2000, where he is currently working toward the Ph.D. degree.

His work is based on the development of advanced numerical modeling tools for the design and optimization of high-brightness tapered lasers.

Michel Krakowski was born in Paris, France, on August 27, 1955. He graduated from the Ecole Supérieure d'Electricité, Gif sur Yvette, France, and received the Diplôme d'Etude Approfondies degree in material sciences from the University of Paris, Paris, France, in 1980.

In 1980, he joined the Central Research Laboratory, Thomson-CSF, Orsay, France, where he has been involved in the characterization and modeling of 0.8- and 1.3-μm high-power laser diodes array, 0.8-μm superluminescent diodes, 1.3-μm buried heterostructure laser diodes, and 1.55-μm multiquantum-well DFB lasers for cable television and microwave applications. He is in charge of the design and characterization of high-power laser diodes. Since 1998, he has been a Member of the Technical Staff, Optronics Devices Laboratory, Thomson-CSF.

Bernd Sumpf was born in Berlin, Germany, in 1958. He received the Dipl. degree in physics and the Ph.D. degree from the Humboldt-Universität, Berlin, Germany, in 1981 and 1987, respectively. His dissertation focused on lead salt diode lasers for spectroscopic applications.

From 1993 to 1997, he was with the Technische Universität Berlin, Berlin, Germany, where he was involved with high-resolution spectroscopy and difference-frequency generation. In 1997, he received the postdoctoral lecture qualification. Since 2000, he has been with the Ferdinand-Braun-Institut for Höchstfrequenztechnik, Berlin, where he has been involved in high-brightness diode lasers.

Phillip Sewell was born in London, U.K., in 1965. He received the B.Sc. degree in electrical and electronic engineering (first class honors) and the Ph.D. degree from the University of Bath, Bath, U.K., in 1988 and 1991, respectively.

From 1991 to 1993, he was an S.E.R.C. Postdoctoral Fellow with the University of Ancona, Ancona, Italy. Since 1993, he has been a Lecturer, and from 2001 a Reader, in the School of Electrical and Electronic Engineering, University of Nottingham, Nottingham, U.K. His research interests involve analytical and numerical modeling of electromagnetic problems, with application to optoelectronics, microwaves, and electrical machines.

Sophie-Charlotte Auzanneau was born in 1974 in France. She received the M.S. degree from the Ecole Nationale Supérieure de Physique Marseille, France, in 1998, and the Ph.D. degree in optoelectronics from the University of Paris XI, Paris, France, in 2002.

Presently she is Member of Technical Staff at THALES Research and Technology, Domain de Corbeville, France, working on high-power laser diodes.

Hans Wenzel received the Dipl. and Ph.D. degrees in physics from Humboldt University, Berlin, Germany, in 1986 and 1991, respectively. His thesis dealt with the electrooptical modeling of semiconductor lasers.

From 1991 to 1994, he was involved in a research project on the three-dimensional simulation of DFB lasers. In 1994, he joined the Ferdinand-Braun-Institut für Höchstfrequenztechnik, Berlin, Germany, where he is engaged in the development of high-power semiconductor lasers including DFB lasers.

Daniel Rodríguez was born in Ferrol, Spain, in 1975. He received the M.S. degree in physics from Universidade de Santiago de Compostela, Santiago de Compostela, Spain, in 1998, and he is currently working toward the Ph.D. degree at the Universidad Politécnica de Madrid, Madrid, Spain.

From 1998 to 2000, he was with the Applied Physics Department, Universidade de Santiago de Compostela. In 2000, he joined the Laser Diode Group, Photonics Technology Department, Universidad Politécnica de Madrid. His current research interests are in high-brightness laser simulation and characterization.

Trevor M. Benson was born in Sheffield, U.K., in 1958. He received the degree in physics (first class honors) and the Ph.D. degree in electronic and electrical engineering from The University of Sheffield, Sheffield, U.K., in 1979 and 1982, respectively.

After spending more than six years as a Lecturer with University College Cardiff, Wales, U.K., he joined the University of Nottingham, Nottingham, U.K., as a Senior Lecturer in Electrical and Electronic Engineering in 1989. He was promoted to the posts of Reader in Photonics in 1994 and Professor of Optoelectronics in 1996. His present research interests include experimental and numerical studies of electromagnetic fields and waves, with particular emphasis on propagation in optical waveguides and lasers, silicon based photonic circuits, and electromagnetic compatibility.

Eric C. Larkins (S'82–M'89) received the B.S.E.E. degree from Cornell University, Ithaca, NY, in 1980 and the M.S.E.E. and Ph.D. E.E degrees from Stanford University, Stanford, CA, in 1985 and 1991, respectively. He pursued his Ph.D. research on light-emitting heterostructure thyristors and molecular beam epitaxy, receiving full support from 1985 as a Kodak Fellow.

From 1991 to 1994, he was a Visiting Scientist with the Fraunhofer Institute for Applied Solid State Physics, Freiburg, Germany, where he worked on high-speed laser diodes, optical modulators, and metal–semiconductor–metal and intersubband photodetectors. He joined the School of Electrical and Electronic Engineering at the University of Nottingham, Nottingham, U.K., as Lecturer in 1994 and was appointed Professor of Optoelectronics in 2002. His current research interests include high-power laser diodes, functional photonics, and new optical materials.

Ignacio Esquivias (M'94) was born in Madrid, Spain, in 1955. He received the M.Sc. and Ph.D. degrees in electronic engineering from the Polytechnical University of Madrid, Madrid, Spain, in 1977 and 1983, respectively.

In 1984, he became an Associate Professor with the Department of Electronic Technology, Polytechnical University of Madrid. From 1990 to 1992, he was a Visiting Scientist with the Fraunhofer Institute for Applied Solid State Physics, Freiburg, Germany. In 1992, he returned to his position at the Polytechnical University of Madrid, becoming Full Professor in 2001 in the Department of Photonic Technology. His research activity has been always related to optoelectronic materials and devices (polycrystalline silicon solar cells, HgCdTe and HgZnTe for infrared detectors). Since 1991, he has been working in characterization and modeling of laser diodes for high-speed and high-power applications.